The following publication L. Dai, S. Niu, X. Yuan and C. C. Chan, "Data-Driven Current Harmonic Optimization for Minimizing Torque Ripple and Injection Losses in PMSM Drives," in IEEE Transactions on Industrial Electronics, vol. 73, no. 3, pp. 4495-4505, March 2026 is available at https://doi.org/10.1109/TIE.2025.3613632.

Data-Driven Current Harmonic Optimization for Minimizing Torque Ripple and Injection Losses in PMSM Drives

Litao Dai, *Member*, *IEEE,* Shuangxia Niu, *Senior Member, IEEE,*
Xin Yuan, *Senior Member, IEEE,* and C. C. Chan, *Life Fellow, IEEE*

***Abstract*—Torque ripple mitigation is a critical topic in the field of permanent magnet machine drives, and current harmonic injection is regarded as an effective approach to address this issue. However, traditional harmonic injection methods heavily rely on model-based calculations that necessitate various precise motor equivalent parameters. Additionally, they struggle to account for the iron loss effect. Furthermore, due to the nonlinear nature of motor parameters, these approaches frequently result in suboptimal torque ripple mitigation and elevated injection losses. To overcome these limitations, this paper proposes a data-driven-based harmonic injection method. In contrast to model-based techniques, the proposed method offers the advantages of independence from motor parameters, unaffected torque ripple reduction by magnetic saturation, and overall minimization of injection copper and iron losses. The key of the proposed method lies in establishing precise correlations between injected current harmonic, torque ripple, and losses through a meta-model. Moreover, a multi-objective optimization process is applied to identify the optimal injection currents, leading to minimizations in torque ripple and injection losses.**

***Index Terms*—Permanent magnet machines, torque, harmonic, loss, optimization.**

I. Introduction

THE electromagnetic torque is a crucial aspect of rotary electric machines, defining the conversion between mechanical and electrical energy. In real-world motor operations, torque often fluctuates cyclically, generating what is known as torque ripple. This ripple can greatly affect performance by impacting operational stability, control precision, and the fatigue of the rotor shaft [1]. Given its significance, reducing torque ripple in electric machines is a key area of research, especially in the domain of permanent magnet synchronous machines (PMSMs) [2]. PMSMs are highly valued for their high-power density and reliability, making them widely applied in various industrial settings [3].

Techniques for mitigating torque ripple generally fall into two categories: motor design-based methods and control-based methods. Design approaches aim to minimize torque ripple by optimizing structural parameters like winding arrangement [4], PM layer shape [5], profiles of rotor core [6] and stator core [7]. While design-based methods have shown effectiveness, they may encounter limitations due to manufacturing deviations and the challenge of achieving effective ripple reduction across all operating conditions.

On the other hand, controlling motor current to mitigate torque ripple offers a versatile solution, effectively addressing torque fluctuations stemming from design and manufacturing discrepancies, applicable across various motor types. Control strategies can be classified into two main pathways: learning control and active harmonic injection. Learning control involves monitoring and adjusting current commands based on torque or speed variation trajectories, employing methods like iterative learning control [8], [9], and repetitive control [10], [11]. Active harmonic injection, another strategy, counteracts design-induced torque ripples by injecting current harmonics, resulting in smoother torque output [12], [13].

However, injecting current harmonics into the *dq*-axis currents inevitably leads to additional losses. Therefore, to effectively minimize torque ripple and decrease harmonic injection losses, optimizing the amplitude and phase of the injected *d*- and *q*-axis currents is crucial.

Analytical solutions based on torque ripple models have been investigated [14], [15], [16], [17], [18], [19] focusing on compensating for inherent torque ripple by introducing minimal *dq*-axis current harmonics. These solutions heavily depend on PMSM equivalent parameters like *dq*-axis inductance and flux linkage, which can be notably affected by motor saturation. As a result, researchers have started integrating saturation effects into these analytical solutions [20]. However, accurate understanding of equivalent parameters under saturation conditions is crucial for effectively applying these analytical techniques, thereby presenting implementation challenges.

Alternatively, a data-driven strategy can bypass the need for precise parameter information. By collecting extensive motor operating data, including details on injected current harmonics and torque ripple, and fitting this data to a surrogate model that

Litao Dai, Shuangxia Niu, and C. C. Chan are with the Department of Electrical and Electronic Engineering, The Hong Kong Polytechnic University, Hong Kong 999077, China (e-mail: litao.dai@polyu.edu.hk; eesxniu@polyu.edu.hk; c.c.chan@polyu.edu.hk). (Corresponding author: Shuangxia Niu.)

Xin Yuan is with the Department of Electronic & Electrical Engineering at the University of Strathclyde, Glasgow G1 1XQ, UK. (e-mail: xin.yuan@strath.ac.uk)

mirrors the motor's behavior. Subsequently, optimization techniques such as genetic algorithm [21] and particle swarm optimization algorithm [22] can be utilized to minimize both torque ripple and current harmonic-induced loss by setting them as objective functions.

Existing injection-based methods, whether analytical or data-driven, primarily focus on minimizing torque ripple and copper loss, often neglecting iron loss. In practical motor applications, iron loss induced by injected current can exceed copper loss due to the heightened frequency of injected current. Ignoring iron loss in current injection strategies could result in amplified energy wastage and equipment heating due to excessive losses.

The neglect of iron loss in existing approaches can be attributed to the following factors:

- Accurately calculating and integrating iron loss into the equivalent *dq*-axis model presents challenges. Achieving precision in quantifying this loss and integrating it into the equivalent *dq*-axis model is inherently complex [23].
- Iron loss follows a nonlinear function based on motor operating conditions, adding complexity into determining the optimal current injection solution for minimization.

Therefore, finding an optimal solution to achieve torque ripple and injected losses minimization is challenging.

Furthermore, as the patterns of losses and torque ripple (both amplitude and phase) might vary notably across different current and speed conditions, traditional single-condition optimization approaches fail to achieve torque ripple and loss minimization across a wide range of torque-speed conditions.

In response to these challenges, this paper proposes a novel data-driven approach to seek for the optimal solution of *dq*-axis current harmonics suitable for a wide range of machine operating conditions. The objective is to concurrently minimize torque ripple, injected copper and iron losses. To accomplish this aim, the paper highlights the following key contributions:

- The numerical model, fine-tuned with experimental data, ensures precise torque and loss data collection. This adjustment expedites subsequent dataset sampling since experiments are solely dedicated to the correction process.
- Implementing a comprehensive procedure, involving the design of experiments (DoE), model fitting, and global optimization, to compute the optimal current trajectory for reducing torque ripple and total injected losses.
- Separate optimization of multiple motor operating points based on the meta-model ensures that the current harmonic trajectories are optimized across a wide range of operating conditions, taking into account issues such as magnetic saturation effects and high-speed iron losses.

The proposed method is well-suited for integrated machine-controller products such as transportation electric drives, power generation equipment, and household appliances. It effectively addresses the common limitations of lengthy calibration times and the difficulty in ensuring global optimality that are prevalent in existing harmonic injection-based torque ripple suppression methods.

The paper is organized as follows: Section II discusses the effects of harmonic injection on torque ripple and losses. Section III introduces the proposed method. Section IV details the optimization process step by step. Section V provides a comparison and validation using the finite-element method (FEM), followed by experimental verification in Section VI. Finally, Section VII concludes the study.

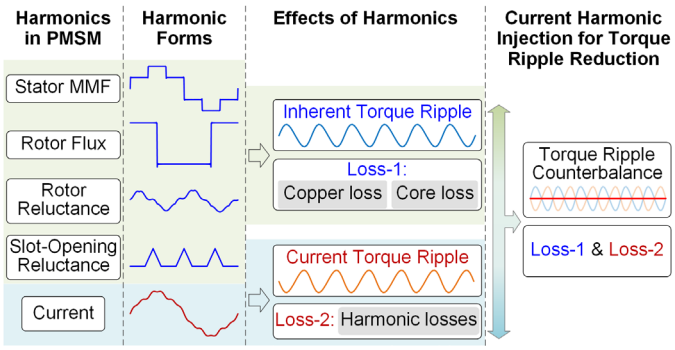

Fig. 1. Illustration of PMSM harmonic forms, torque ripple sources, and the principle of current harmonic injection method.

II. Analysis of the Effects of Current Harmonics on Torque Ripple and Losses

In order to provide a comprehensive understanding of the harmonic forms in PMSM, the causes of torque ripple, and the principle of current harmonic injection method, a schematic diagram is presented in Fig. 1. This diagram illustrates that despite sinusoidal current excitation; torque ripple remains inherent in PMSMs owing to the persistence of various spatial harmonic forms. The interaction of these harmonics leads to different types of torque ripple, including cogging torque, synchronous torque ripple, and reluctance torque ripple [6]. Although the sources of ripple are complex, the resulting torque ripple pattern in three-phase PMSMs is typically characterized by the 6n-th electrical frequency [6]. Fortunately, this inherent torque ripple can be mitigated through specialized current harmonic configurations, effectively balancing out the ripple. Nevertheless, additional losses stemming from the current harmonics are inevitable. These relationships will be thoroughly examined in the subsequent section.

A. Effect of Current Harmonics on Torque Ripple

The electromagnetic torque of three-phase PMSMs under sinusoidal current excitation can be expressed as follows:

$$T_{\mathrm{e}} = \sum_{k=0,6,\ldots,6n} T_{\mathrm{ek}}(k)\sin\left(k\theta_{\mathrm{e}} + \varphi_{\mathrm{ek}}(k)\right) \tag{1}$$

where k, $T_{\mathrm{ek}}(k)$, $\varphi_{\mathrm{ek}}(k)$ represent the frequency, amplitude, and phase of the k -th harmonic of torque, and θ_{e} is the electrical rotor position. It is observed that the machine exhibits torque ripple frequency in $6n$ form, where $k=0$ represents the DC component, and $k=6,12,\ldots,6n$ represents the torque ripples generated by the inherent spatial harmonics in PMSM.

From the viewpoint of the field-oriented control for three phase PMSMs, the relationship between *dq*-axis currents and torque is described as:

$$T_{\mathrm{C}} = 1.5p_{\mathrm{N}}\left(\psi_{\mathrm{m}} + L_{\Delta}i_{\mathrm{d}}\right)i_{\mathrm{q}} \tag{2}$$

where p_{N} and ψ_{m} represent the pole-pairs number and rotor flux-linkage, while i_{d}, i_{q} are the *d*- and *q*- axis currents. L_{Δ} signifies the inductance difference between the *d*- and *q*- axes.

In (2), if the i_{d}, i_{q} consist only of DC components, then the

T_C remains constant. Thus, to generate a pulsating torque capable of counterbalancing the torque ripple illustrated in (1), the i_d, i_q must incorporate AC components following a $6n$ pattern in frequency. The expression of i_d, i_q is as follows:

$$\begin{cases} i_d = \sum_{k=0,6,\ldots,6n} I_{dk}(k)\sin\left(k\theta_e + \varphi_{dk}(k)\right) \\ i_q = \sum_{k=0,6,\ldots,6n} I_{qk}(k)\sin\left(k\theta_e + \varphi_{qk}(k)\right) \end{cases} \tag{3}$$

where $I_{dk}(k)$, $\varphi_{dk}(k)$, $I_{qk}(k)$, and $\varphi_{qk}(k)$ are the amplitude and phase of the k-th frequency of i_d and i_q currents.

By substituting (3) into (2), and disregarding the DC torque component, the resulting k-th torque ripple induced by the current harmonic can be expressed as follows:

$$T_{C.k} = T_{k1} + T_{k2} + T_{k3} = T_{Ck}(k)\sin\left(k\theta_e + \varphi_{Ck}(k)\right) \tag{4}$$

and

$$\begin{cases} T_{k1} = 1.5p_N\psi_m I_{qk}(k)\sin\left(k\theta_e + \varphi_{qk}(k)\right) \\ T_{k2} = 1.5p_N L_\Delta I_{d0}(0) I_{qk}(k)\sin\left(k\theta_e + \varphi_{qk}(k)\right) \\ T_{k3} = 1.5p_N L_\Delta I_{q0}(0) I_{dk}(k)\sin\left(k\theta_e + \varphi_{dk}(k)\right) \end{cases}$$

where $T_{Ck}(k)$ and $\varphi_{Ck}(k)$ are the amplitude and phase of the k-th injected torque ripple. Despite the intricate components of T_{k1}, T_{k2}, and T_{k3}, the finalized ripple frequency adheres to the $k = 6n$ pattern with the ripple conditions of $T_{Ck}(k)$ and $\varphi_{Ck}(k)$. Notably, these ripple conditions are closely related to the parameters of *dq*- axis current harmonics, i.e., $I_{dk}(k)$, $\varphi_{dk}(k)$, $I_{qk}(k)$, and $\varphi_{qk}(k)$.

To achieve torque ripple counterbalancing, combine (1) and (4) and ensure the following conditions are met:

$$T_{Ck}(k) = -T_{ek}(k), \quad \varphi_{Ck}(k) = \varphi_{ek}(k) \tag{5}$$

Moreover, to minimize additional copper loss, the current harmonic should satisfy the condition:

$$\min: \quad f = \sqrt{I_{dk}^2(k) + I_{qk}^2(k)} \tag{6}$$

It is a common optimization challenge in the Lagrangian framework to minimize the injecting copper loss as per (6) while ensuring torque ripple elimination as specified in (5). Several insightful studies have delved into analytically determining the optimal solutions for the injecting current parameters ($I_{dk}(k)$, $\varphi_{dk}(k)$, $I_{qk}(k)$, $\varphi_{qk}(k)$) as follows:

$$\begin{aligned} &\text{In Refs. [15],[16]:} \quad I_{dk} = \frac{L_\Delta I_{q0}}{(\psi_m + L_\Delta I_{d0})} I_{qk}, \varphi_{dk} = \varphi_{qk} \\ &\text{In Ref. [20]:} \quad I_{dk} = \frac{L_\Delta I_{q0}}{(\psi_m + L_\Delta I_{d0} + 2L_{dq} I_{q0})} I_{qk}, \varphi_{dk} = \varphi_{qk} \end{aligned} \tag{7}$$

where L_{dq} denotes the mutual inductance between *d*- and *q*-axes. In (7), both solutions simplify the optimization of *dq*-axis currents by reducing the number of current parameters from four to two. The remaining two parameters are then dictated by the specific torque ripple amplitude $T_{ek}(k)$ and phase $\varphi_{ek}(k)$ conditions. Notably, these amplitude and phase values vary under different current conditions, underscoring the need for precise torque data acquisition. Furthermore, the optimal relationships in (7) requires accurate torque and PMSM parameters, including L_Δ, ψ_m, I_{q0}, I_{d0}, and L_{dq}.

Hence, achieving copper loss minimization and torque ripple elimination necessitates comprehensive consideration of motor conditions and equivalent parameters. It's essential to note that in these solutions, the impact of iron loss has been disregarded.

B. Effect of Current Harmonics on Losses

Previous studies [14], [15], [16], [17], [20] have assumed that meeting condition (6) leads to minimized current loss. However, this conclusion is only applicable to the *dq*-axis model. In a practical three-phase model, the $6n$-th *dq*-axis currents can produce both the $(6n\text{-}1)$-th and $(6n\text{+}1)$-th harmonics with varied amplitudes in the windings. The resulting winding currents for the *k*-th injected *dq*-axis currents can be expressed as:

$$i_{mk}(m) = i_{m,k+1}(m) + i_{m,k\text{-}1}(m), \quad m = 1,2,3 \tag{8}$$

$$\begin{aligned} i_{m,k+1}(m) = &\frac{1}{3}\left[I_{dk}\cos\varphi_{dk} - I_{qk}\sin\varphi_{qk}\right]\sin\left(\left(k+1\right)\theta_e - \left(m-1\right)\frac{2\pi}{3}\right) + \\ &\frac{1}{3}\left[I_{dk}\sin\varphi_{dk} + I_{qk}\cos\varphi_{qk}\right]\cos\left(\left(k+1\right)\theta_e - \left(m-1\right)\frac{2\pi}{3}\right) \\ i_{m,k\text{-}1}(m) = &\frac{1}{3}\left[I_{dk}\cos\varphi_{dk} + I_{qk}\sin\varphi_{qk}\right]\sin\left(\left(k-1\right)\theta_e + \left(m-1\right)\frac{2\pi}{3}\right) + \\ &\frac{1}{3}\left[I_{dk}\sin\varphi_{dk} - I_{qk}\cos\varphi_{qk}\right]\cos\left(\left(k-1\right)\theta_e + \left(m-1\right)\frac{2\pi}{3}\right) \end{aligned}$$

where $i_{m,k+1}$ and $i_{m,k+1}$ represent the $(k\text{+}1)$-th and $(k\text{-}1)$-th harmonics in the phase windings, respectively. Their values are influenced by the amplitude and phase of the *dq*-axis currents.

Furthermore, these winding current harmonics contribute to copper and iron losses. Their relationships are as follows:

$$\begin{aligned} P_{CuH} &= \sum_{k_i = 6n\pm1} 3I_{m,k_i}^2 R_{ph} \\ P_{FeH} &= \sum_{k_i = 6n\pm1} \left[A_e\left[B_c(I_{m,k_i})\right]^2\left(k_i f\right)^2 + A_h\left[B_c(I_{m,k_i})\right]^2\left(k_i f\right)\right]V_C \end{aligned} \tag{9}$$

where k_i is the frequency of winding currents, with k_i=$6n\pm1$. I_{m,k_i} is the amplitude of k_i-th current, R_{ph} is the phase resistance, $B_c(I_{m,k_i})$ is the flux density in the iron core generated due to the k_i-th current, f is the electrical frequency, and A_e, A_h are the coefficients of eddy current loss and hysteresis loss, respectively. V_C is the volume of the iron core.

From (9), it is evident that the iron loss is more intricate and potentially more significant than copper loss due to the substantial impact of the harmonic frequency on iron loss, following power levels of 1 to 2. Traditional studies have frequently overlooked iron loss, given that the *dq*- axis model fails to account this winding harmonic effect. Additionally, accurately predicting the factors A_e and A_h poses challenges.

Fig. 2 illustrates the additional copper and iron losses due to harmonic injection in the studied PMSM to mitigate torque ripple, as derived from the FEM analysis. The results emphasize the significant impact of current harmonics on iron losses compared to copper losses under rated torque and varying speeds. Overall, identifying the optimal solution to effectively reduce torque ripple while minimizing overall losses presents analytical challenges.

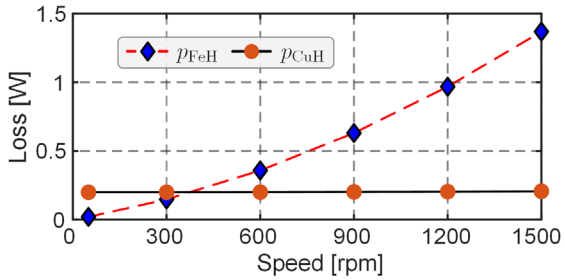

Fig. 2. Illustration of additional copper and iron losses due to harmonic injection.

III. Method Presentation

The preceding analysis highlights the challenge of reducing torque ripple while minimizing current harmonics-induced losses through model-based methods. This section proposes a data-driven approach to solve this nonlinear multi-objective optimization problem and details the necessity and implementation of each step.

Fig. 3 shows the schematic diagram of the proposed data-driven approach. In general, the method consists of three key steps: 1) numerical model correction; 2) meta-model construction; 3) multiple conditions optimization. The functions of each step are illustrated in the subsections, with specific implementation discussed in Section IV.

A. Numerical Model Correction

To address a nonlinear optimization problem, a model that can predict input and output characteristics is essential. The accuracy of the model directly influences the effectiveness of the optimization results. FEM is a preferred option for forecasting machine torque and losses under diverse operational scenarios. While FEM excels at accurately predicting copper loss by considering AC effects, it often struggles to predict iron loss with the same precision.

To overcome this limitation, experimental data is gathered to refine the FEM iron loss model, enhancing its suitability for predicting torque and losses effectively.

Fig. 4 shows the energy flow, power measuring method, and losses separation method of the investigated motor system. The power balancing equation is presented as follows:

$$P_{\mathrm{In}} = P_{\mathrm{Out}} + p_{\mathrm{Cu}} + p_{\mathrm{Fe}} + p_{\mathrm{pwm}} + p_{\mathrm{ad}} \tag{10}$$

where P_{In}, P_{Out}, p_{Cu}, p_{Fe}, p_{pwm}, p_{ad} represent input power, output power, copper loss, iron loss, inverter supply and switching loss, and additional loss, respectively. P_{In} and P_{Out} are measured by power analyzer and torque transducer, while p_{Cu} is calculated based on measuring current and resistance. p_{pwm} and p_{ad} are determined at low-speed testing, where iron loss can be disregarded in this condition. Consequently, the remaining loss is classified into iron loss. By fitting the FEM model into the test iron loss data under variable speed conditions, the iron loss coefficients in the FEM model can be corrected.

B. Meta-Model Construction

The refined FEM model will be further utilized as the base model to generate a dataset, which will then be used to train a meta-model for optimization purposes. The FEM model is not directly employed as the optimization model due to the computational intensity required for optimization involving a large number of cases to cover various operating conditions. Conversely, a meta-model, serving as a fitting model, offer rapid computational speeds, effectively addressing this challenge, thereby significantly accelerating the optimization process. However, it is important to ensure the fidelity of the meta-model to ensure the optimization effectiveness.

Fig. 5 shows the proposed meta-model construction process. The initial step involves generating a comprehensive sampling matrix that spans the entire parameter range, necessitating the use of DoE. Subsequently, each motor case within the sampling

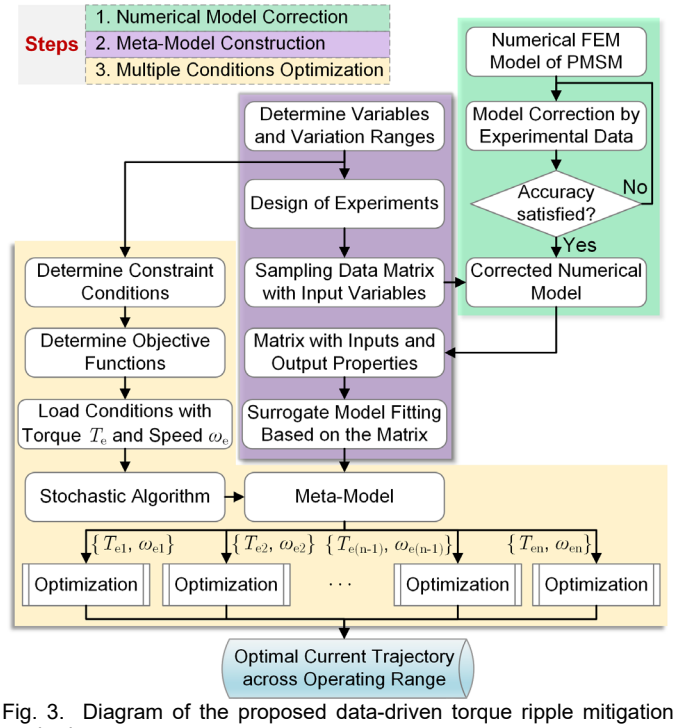

Fig. 3. Diagram of the proposed data-driven torque ripple mitigation method.

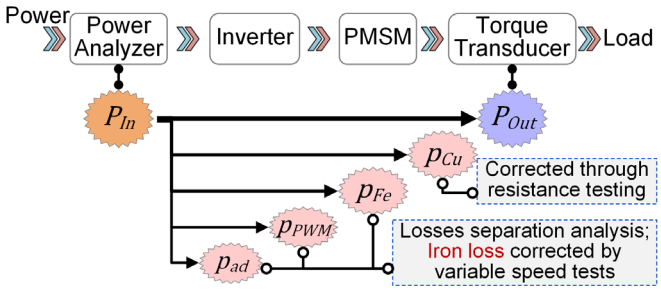

Fig. 4. Energy flow and measuring method of the motor driving system.

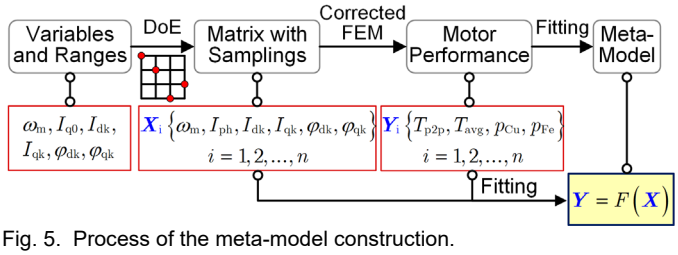

Fig. 5. Process of the meta-model construction.

matrix undergoes analysis using the corrected FEM model to acquire torque and loss data. This data is then utilized to train a meta-model that serves as a surrogate for the FEM model.

C. Multiple Conditions Optimization

The final stage involves conducting iterative optimization to determine the optimal current injection parameters for reducing torque ripple while minimizing losses. A visual representation of this stage is provided in Fig. 6.

From Fig. 6, it can be observed that optimization is repeatedly performed across multiple operating conditions, yielding different solutions. This necessity arises from the fact that torque ripple and losses vary with changing operating conditions, leading to different current harmonic solutions for each condition. Fortunately, even with a large number of optimizations to be conducted, meta-model can significantly accelerate this process.

Ultimately, this method generates a solution set for the injecting current that is applicable across the entire operational spectrum, offering an optimal trajectory for current harmonic injection.

IV. Method Implementation

To offer a clearer explanation of the proposed method, this section provides a step-by-step implementation aligned with the optimization process detailed in Section III.

A. Numerical Model Correction

Three machine performance indicators need to be analyzed using the FEM model: torque, copper loss, and iron loss.

Initially, torque correction can be achieved by adjusting the structural model in FEM to mirror actual motor manufacturing processes. These structural adjustments include modifications such as chamfering of PMs, adjusting the plating gap between the PMs and the core.

Additionally, correcting copper loss is straightforward by offline measurement of winding resistance.

The most challenging task in this stage is correcting iron loss. In this study, a loss separation analysis is conducted. Referring to (10), when the motor is operated at low speed, the iron loss can be ignored, allowing for the determination of the inverter loss and additional loss. Consequently, all losses except iron loss are meticulously calibrated.

Subsequently, the PMSM is operated at various speeds to record the overall losses and compute the iron losses. A comparison between the FEM-predicted and measured iron losses is then carried out to determine the amplification factor required for adjustment in the corrected FEM model. After these corrections, the comparison between the FEM and measured iron losses is illustrated in Fig. 7, demonstrating a notable improvement in fitting accuracy. The corrected FEM model will be further used as the base model for subsequent dataset collection, and its accuracy characteristic can ensure the reliability of the dataset.

B. Meta-Model Construction

It is crucial to comprehensively collect datasets on input parameters and output performance. Optimal Latin Hypercube Sampling (OLHS) [24], as an advanced and widely used DoE

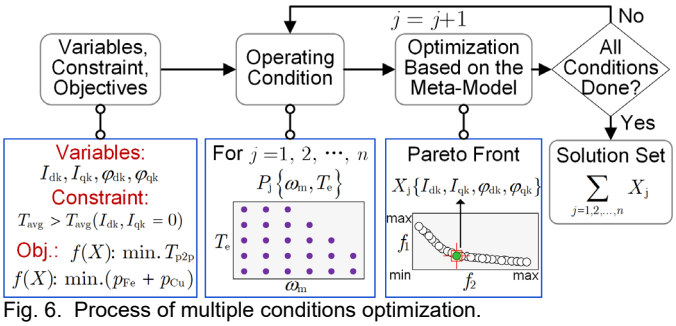

Fig. 6. Process of multiple conditions optimization.

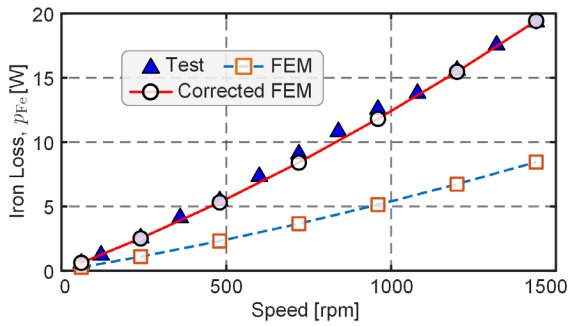

Fig. 7. Comparison between the tested, FEM-predicted, corrected FEM calculated iron losses.

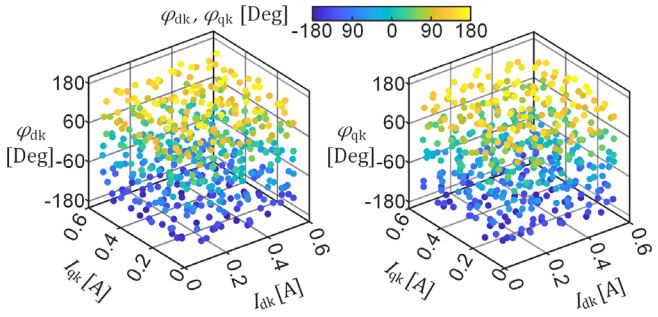

Fig. 8. The 3D scattered plots of the DoE samplings: (a) φ_{dk} with respect to I_{dk} and I_{qk}. (b) φ_{qk} with respect to I_{dk} and I_{qk}.

method, achieves the objective of capturing a wide range of data features using a minimal number of points. This is accomplished through a hierarchical approach that guarantees the uniform distribution of sampling points across the design variable range.

In this study, the input parameters include motor speed (ω_m), the DC component of q-axis current (I_{q0}), and the amplitude and phase of the injected dq-axis currents (I_{dk} , I_{qk} , φ_{dk} , φ_{qk}). Recognizing the significant impact of motor speed on iron loss, a hybrid OLHS strategy is implemented, managing four parameters (I_{dk} , I_{qk} , φ_{dk} , φ_{qk}) in a matrix with 500 randomized samples. Three-dimensional (3D) scattered plots of these samplings are depicted in Fig. 8, illustrating the interrelations among the input parameters. Notably, the sampling points are evenly distributed across variation ranges, facilitating comprehensive information gathering.

Subsequently, this sampling matrix is computed iteratively for speed points of 50, 500, 1000, 1500 rpm, and I_{q0} points of 0, 1, 2, 3, 4, 5 A, resulting in a total of 12,000 samples. The

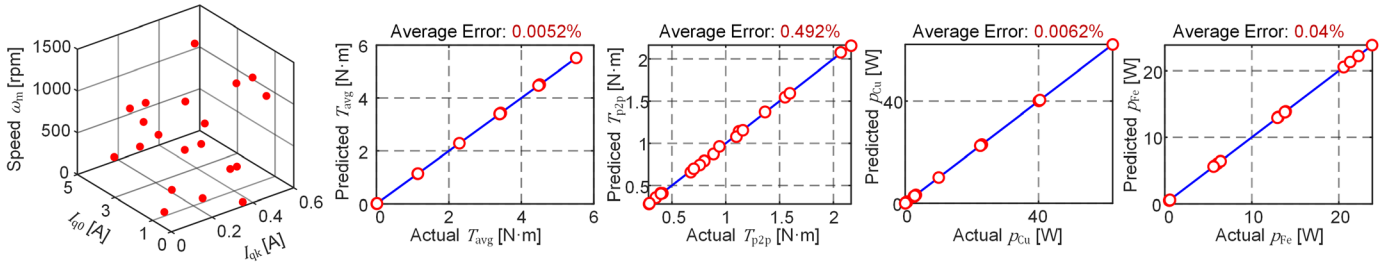

(a) (b) (c) (d) (e)

Fig. 9. Cross-validation error analysis. (a) 3D distribution of the cross-validation samples. (b) Error analysis of average torque. (c) Error analysis of Torque ripple. (d) Error analysis of copper loss. (e) Error analysis of iron loss.

output metrics to be evaluated include average torque T_{avg}, torque ripple T_{p2p} (peak-to-peak of torque), copper loss p_{Cu}, and iron loss p_{Fe}.

After conducting FEM calculations on all samples, the resulting matrix is fed into an Elliptical Basis Function Neural Network (EBFNN) for meta-model approximation. The EBFNN is adept at addressing nonlinear problems owing to its flexible basis function shapes [25]. Given the pronounced nonlinear nature of torque ripple and losses, this method is selected for approximation. The EBFNN training parameters include a smoothing filter set at 0.08 and a maximum of 20 iterations used to fit an EBFNN model for each response. These settings are guided by the feedback on the approximation accuracy.

To assess the approximation accuracy, cross-validation error analysis is employed, with 20 samples chosen. A 3D plot displaying the three most critical input parameters of these samples is depicted in Fig. 9(a). The actual and predicted output metrics (T_{avg}, T_{p2p}, p_{Cu}, p_{Fe}) for these samples are illustrated in Fig. 9(b), (c), (d), and (e). The comparison reveals highly accurate approximation results, with average errors of 0.0052%, 0.492%, 0.0062%, and 0.04%, respectively.

The resulting meta-model can accurately and quickly predict motor performance, which provides the basis for stochastic optimization and greatly speeds up the optimization process.

C. Multiple Conditions Optimization

The optimization necessitates multiple implementations across various torque and speed conditions. These conditions are discretized and grouped into distinct levels. The defined points $C(\omega_{\text{m}}, I_{\text{q0}})$ are presented as:

$$C(\omega_{\text{m}}, I_{\text{q0}}), \quad \begin{cases} I_{\text{q0}} \in [1, \quad 3, \quad 5] \\ \omega_{\text{m}} \in [50, \quad 500, \quad 1000, \quad 1500] \end{cases} \tag{11}$$

The design variables and variation ranges are defined as:

$$I_{\text{dk}}, I_{\text{qk}} \in [0, 0.6]\text{A}, \quad \varphi_{\text{dk}}, \varphi_{\text{qk}} \in [-\pi, \pi] \tag{12}$$

A constraint condition is set to ensure the current harmonic injection does not compromise the average torque. This implies that the average torque does not decrease after harmonic injection compared to no injection, as defined by:

$$Sub.\ to: \quad T_{\text{avg}}(X) > T_{\text{avg}}(I_{\text{dk}} = 0, I_{\text{qk}} = 0) \tag{13}$$

The optimization objectives include minimizing losses and peak-to-peak torque ripple, as shown below:

$$Obj1: \min(p_{\text{Cu}} + p_{\text{Fe}}); \quad Obj2: \min T_{\text{p2p}} \tag{14}$$

To realize multi-objective optimization, NSGA-II is adopted for its efficacy in addressing this challenge [26]. The algorithm parameters are configured as follows: 200 generations, a population size of 100, a crossover probability of 0.8, a crossover distribution index of 10, and a mutation distribution index of 50. Through multi-objective optimization, the Pareto fronts for the 12 operating conditions in (11) are generated, and the results are shown in Fig. 10. It is noteworthy that the criteria for selecting the optimal solution from Pareto fronts include: 1) ensuring torque ripple does not exceed 0.15 Nm, with this value chosen to ensure that the ripple is less than 5% at rated points, and 2) maintaining a balance between average torque and losses. In some Pareto fronts, the losses are significantly lower than nearby points, and these points have been selected.

After 12 optimization procedures, 12 sets of current harmonic solutions were obtained. These 12 sets of solutions can be further fitted to create an optimal surface covering all torque and speed ranges. The current parameters corresponding to these 12 scatter points and their fitted surface are shown in Fig. 11, where (a), (b), (c), and (d) correspond to the 3D distribution patterns of I_{dk}, I_{qk}, φ_{dk}, φ_{qk} regarding the torque-speed range.

D. Highlights of the Optimization Process

In the above, a comprehensive methodology for determining the optimal current harmonics to minimize torque ripple and injected losses is elaborated in detail. The distinctive features of the proposed methods are outlined as follows:

In comparison with the model-based approach, the proposed data-driven technique offers the following advantages: 1) enhanced optimization outcomes for torque ripple and injecting losses by considering iron loss effects and employing global stochastic optimization; 2) effectiveness across all torque-speed operating conditions through the utilization of multi-conditions optimization and the incorporation of motor saturation effects via the refined high-fidelity FEM predictions.

When compared to the practical testing calibration method, the proposed method presents the following benefits: 1) substantial reduction in calibration time by employing a combination of DoE, high-precision fitting, and optimization techniques; 2) improved torque ripple and losses minimization as real-world testing often struggles to precisely measure torque ripple, particularly under high-speed conditions, a challenge overcome by the corrected FEM model.

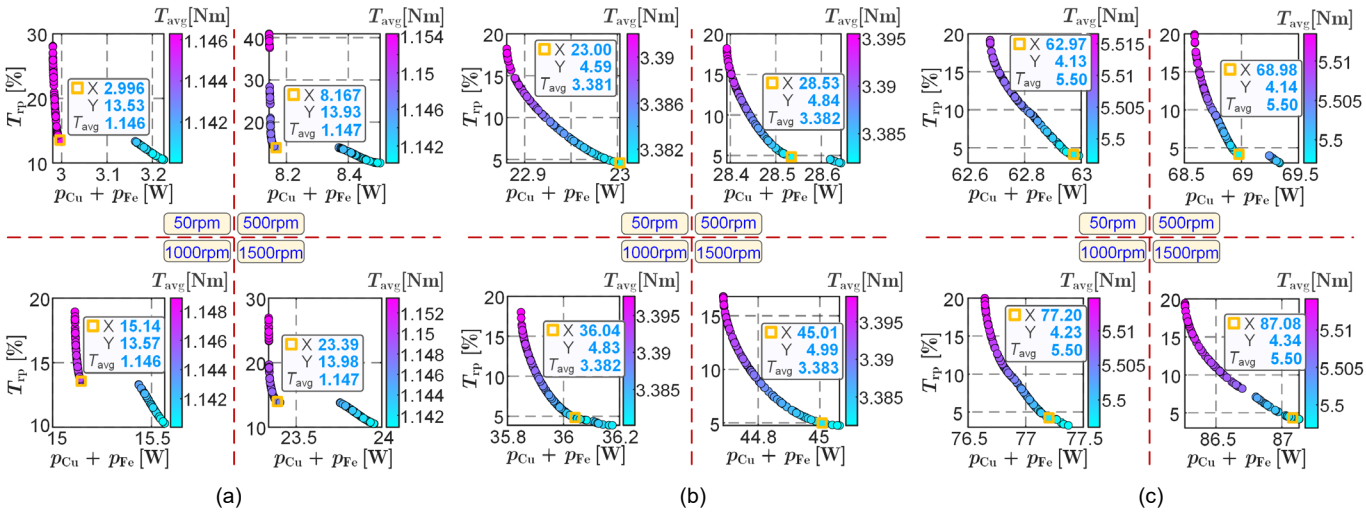

Fig. 10. Pareto fronts of multi-objective optimization under various operating conditions. (a) I_{q0}=1 at different speeds. (a) I_{q0}=3 at different speeds. (c) I_{q0}=5 at different speeds.

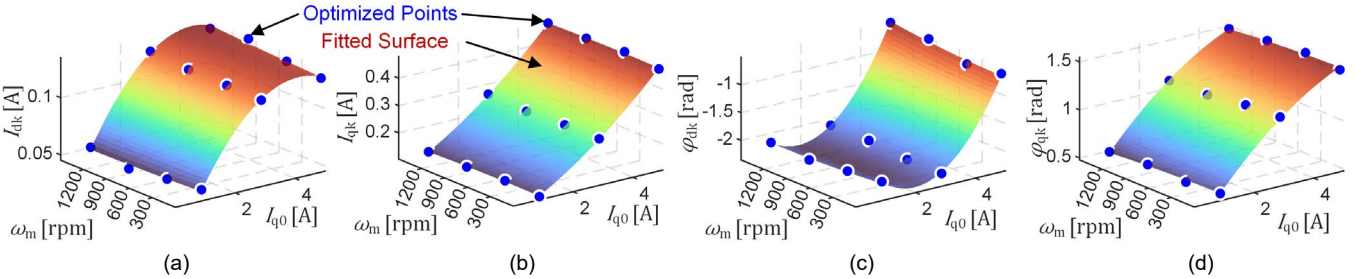

Fig. 11. Optimized solution points and fitted surfaces for injection current parameters over operating ranges. (a) I_{dk}. (b) I_{qk}. (c) φ_{dk}. (d) φ_{qk}.

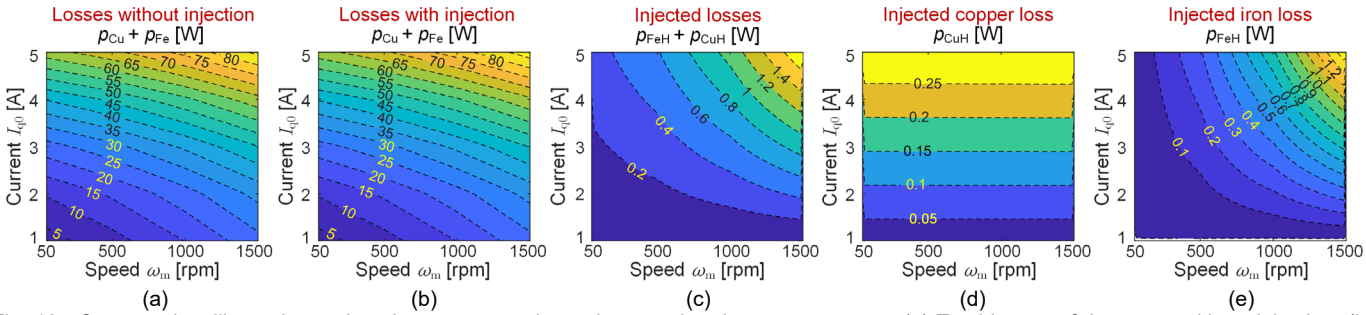

Fig. 12. Contour plots illustrating various losses across the entire speed and torque spectrum. (a) Total losses of the motor without injection. (b) Total losses of the motor with injection. (c) Total losses due to injection. (d) Copper losses from injection. (e) Iron losses from injection.

V. FEM VERIFICATION

To validate the effectiveness of the proposed method, a verification based on FEM simulation was performed. Since the data source for the multi-objective optimization stems from FEM simulations, and considering the inherent high fidelity of FEM, using it for validation is considered reliable.

The FEM verification consisted of two current control sets: one with conventional sinusoidal current excitation and another involving both fundamental and harmonic injection. Each set of simulations encompassed multiple operating conditions with varying torques and speeds. Notably, the solutions of the harmonic injection simulation were derived from the optimization surface, as presented in Fig. 11.

For a visual representation of motor losses with and without harmonic injection across diverse operating conditions, 3D contour plots illustrating various losses for both sets of motor simulations throughout the torque and speed range are presented in Fig. 12. From (a) and (b) in Fig. 12, there appears to be no significant disparity in total motor losses pre- and post-harmonic injection. Specifically, the distinctions in losses pre- and post-injection, inclusive of total injecting losses, injecting copper losses, and injecting iron losses, are elucidated in (c), (d), and (e) in Fig. 12, respectively. It is worth noting that there is negligible variance in copper losses across the entire operational spectrum, with a marginal increase of merely 0.3W at a 120% load condition. Conversely, the addition in iron losses is more noticeable, peaking at an additional 1.3W under maximum torque and speed conditions. Nonetheless, the overall rise in losses remains insignificant, with the highest increase accounting for only 1.28% of the total losses.

On the other hand, concerning torque ripple suppression, Fig. 13 shows a comparison of multi-load torque before and after harmonic injection. It can be seen that effective suppression across various torque conditions is achieved after injection, ensuring smooth motor operation with low torque ripple.

VI. Test Validation

A. Motor Control Strategy and Test Platform

Fig. 14 presents the block diagram of the control strategy for testing PMSM. It can be observed that, based on speed-current dual-loop field-oriented control, additional harmonic currents need to be injected in the d- and q- axes to suppress torque ripple. The command for harmonic currents is calculated based on optimized surface functions shown in Fig. 11 and real-time operational data (ω_{m}, i_{q0}, and θ_{r}).

Furthermore, to achieve precise control for the current harmonics, a quasi-proportional-resonant (QPR) controller is utilized. This controller inherits the high bandwidth response capability of the proportional-resonant (PR) controller, ensuring accurate amplitude and phase control of current harmonics while mitigating the narrow resonant bandwidth constraint often seen in PR control [27]. Hence, this controller not only exhibits outstanding harmonic control capabilities but also effectively prevents deterioration in dynamic performance.

Motor parameters are as follows: 24 slots and 4 poles; a DC-bus voltage of 270V and a rated speed of 1500rpm; a flux linkage of 0.415Wb; a phase resistance of 1.66Ohm; and d- and q-axis inductances of 14.3mH and 40.9mH.

The motor test platform, as shown in Fig. 15, comprises the analyzed PMSM, DSP28335-based motor controller, magnetic powder brake load, torque transducer, power analyzer, and oscilloscope. Notably, to ensure accurate torque measurement, a measurement kit comprising high-precision torque transducer, anti-interference junction box, and signal amplifier is utilized to reduce data acquisition errors and disturbances.

During operation, the input power to the motor system is measured by the power analyzer, while the torque and output power are measured by the torque transducer. This setup enables the determination of the motor's torque and losses during operation.

B. Static Performance

The validation of the motor's static performance focuses on the effectiveness of the proposed method in suppressing torque ripple under various typical operating conditions, specifically at 25% ($I_{q0} = 1A$), 50% ($I_{q0} = 2A$), 100% ($I_{q0} = 4A$), and 125% ($I_{q0} = 5A$) of the rated torque. The outcomes depicting the motor's three-phase currents and shaft torque waveforms under sinusoidal current excitation and harmonic injection conditions are presented in Fig. 16. These results showcase pronounced torque ripples during sinusoidal current excitation, which significantly diminish upon the introduction of harmonic currents, demonstrating notable improvements across multiple loading conditions. Crucially, the transition from sinusoidal excitation to harmonic injection does not induce abrupt fluctuations in phase current and torque.

C. Dynamic Performance

The validation of the motor's dynamic performance focuses on assessing the effectiveness of the proposed method under switching between harmonic injection and non-injection states, as well as under varying load torques, aiming to determine whether the motor exhibits any dynamic disturbances.

The validation comprises three sets of experiments. Firstly, current injection switching at rated load is shown in Fig. 17(a). Subsequently, experiments involve the motor descending from 100% load to 50% load after harmonic injection, and dropping from 100% load to 0% load, with results shown in Figs. 17(b) and (c) respectively. Notably, in addition to torque and phase current, the given and actual q-axis currents are also included in these waveforms. From Fig. 17, it can be observed that neither the harmonic injection switching nor the operation under varying loads resulted in abrupt changes in the phase current, q-axis current, or shaft torque. This suggests that the method does not lead to a deterioration in the motor's dynamic performance. Moreover, based on the behavior of the given and actual q-axis currents, it is evident that QPR control can effectively achieve harmonic current control. Furthermore, the proposed method demonstrates sustained effectiveness in suppressing torque ripples under varying load conditions.

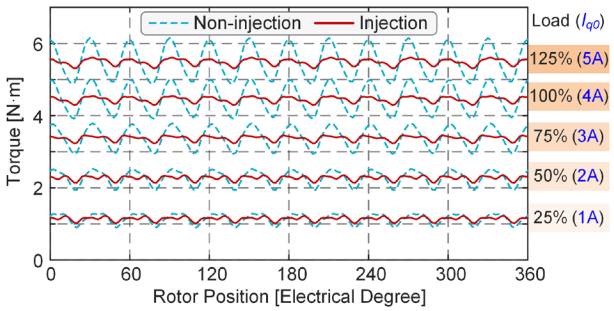

Fig. 13. Comparison of multi-load torque with and without injection.

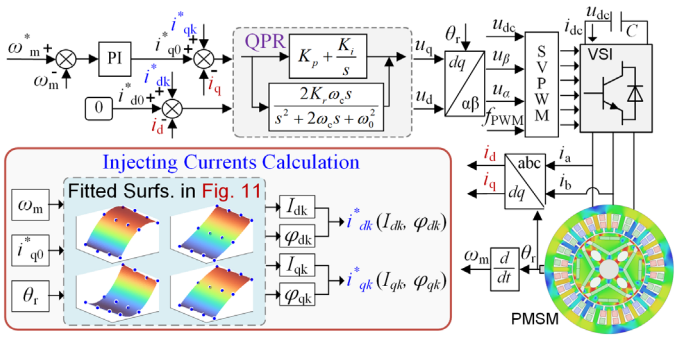

Fig. 14. Block diagram of the motor control strategy.

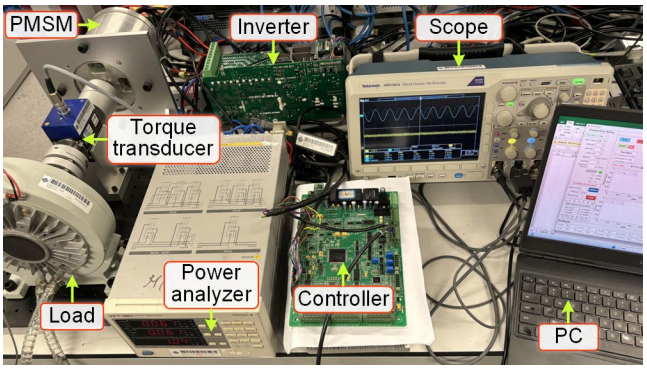

Fig. 15. Motor testing platform.

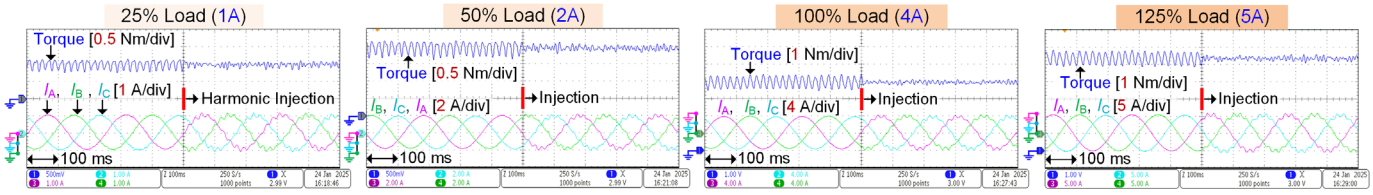

Fig. 16. Waveforms depicting the influence of the proposed current harmonic injection method on shaft torque and phase currents under different torque loads. (a) 25% Load. (b) 50% Load. (c) 100% Load. (d) 125% Load.

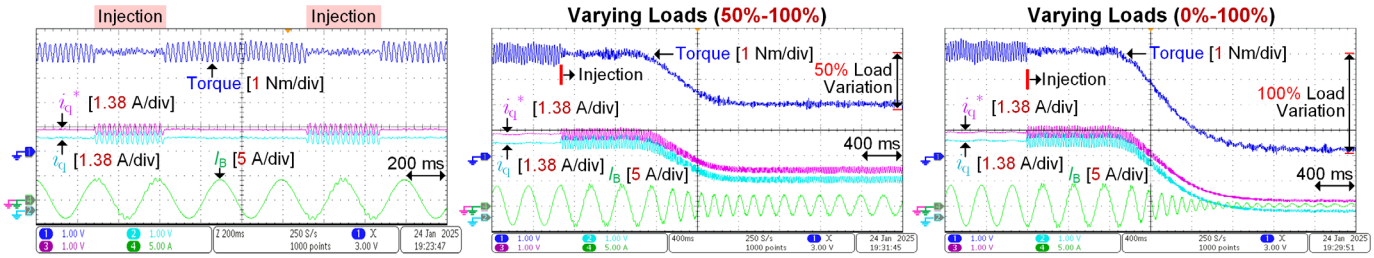

Fig. 17. Waveforms illustrating the impact of the proposed method on various motor dynamic processes. (a) Repetitive current harmonic injection switching. (b) Harmonic injection and load descent from 100% to 50%; (c) Harmonic injection load descent from 100% to 0%.

D. Comparison with Other Advanced Methods

Finally, it is crucial to compare similar methods to validate the superiority of the proposed approach. In direct comparison with this study are model-based methods, with advanced techniques including the solutions proposed in Refs. [15], [16], and [28]. The advantage of model-based solutions lies in their capability to find the specific harmonic solution for minimizing torque ripples. However, these methods require detailed torque ripple and model parameter information and are difficult to account for minimal overall losses. Fig. 18 shows the effects of torque ripple suppression using both the model-based method (in Refs. [15] and [16]) and the proposed data-driven method. The comparison reveals that both methods significantly suppress torque ripples, with slight variations in the magnitude of suppression effects. However, the model-based method requires a larger q-axis current, implying higher losses.

Moreover, this paper conducts a comparative analysis of the injection losses at varying speeds and around the rated torque level among the methods presented in Refs. [15], [16], [28], with results depicted in Fig. 19. To ensure measurement accuracy, the test captures power over a continuous period and calculates the average. It is clear that the proposed method holds superiority in mitigating excessive injected losses.

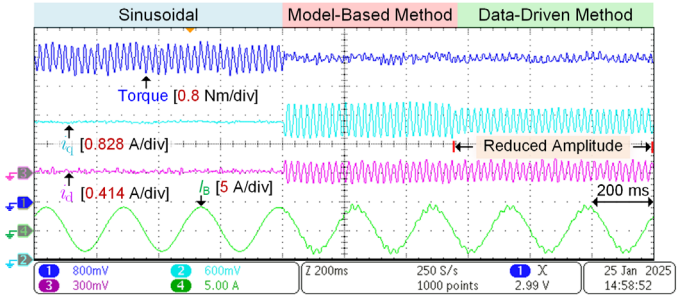

Fig. 18. Comparison of torque ripple and current effects between the model-based method (in Refs. [15], [16]) and the proposed method.

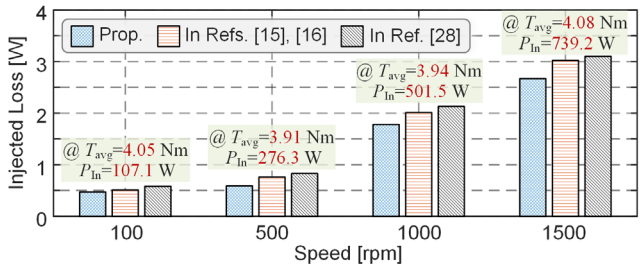

Fig. 19. Comparison of measured injection losses by different methods.

VII. Conclusion

The paper proposes a data-driven harmonic injection method for torque ripple mitigation, which offers the following unique advantages over conventional model-based approaches:

1. The current solution can suppress torque ripple across all load conditions without the need for precise measured torque information and motor equivalent parameters.
2. The current solution avoids excessive injection losses and is applicable across the entire torque-speed operating range.
3. The method can account for magnetic saturation effects and determine the solution under motor parameter nonlinearities, a challenge that model-based methods struggle to address.

Based on the above features, the proposed method is ideally suited for integrated machine-controller electric drives and power generation equipment. It enables the effective determination of the optimal current harmonic trajectory, ensuring stable machine operation with low torque pulsation and reduced losses.

Furthermore, data-driven methods not only tackle torque ripple and harmonic losses minimization but also offer potential applications in control parameter design, system efficiency maximization, fault diagnosis, and fault tolerance. Areas for further exploration include optimizing current trajectory for multifaceted performance enhancements, optimizing switching modulation, precise fitting using limited sampling data, and real-time data collection with iteration strategies. Prospective data-driven approaches will free motor operations from model parameter dependencies and effectively address various unknown challenges.

REFERENCES

[1] F. Barrero and M. J. Duran, "Recent advances in the design, modeling, and control of multiphase machines—part I," *IEEE Trans. Ind. Electron.*, vol. 63, no. 1, pp. 449-458, Jan. 2016.

[2] M. S. Rafaq, W. Midgley and T. Steffen, "A review of the state of the art of torque ripple minimization techniques for permanent magnet synchronous motors," *IEEE Trans. Ind. Inform.*, vol. 20, no. 1, pp. 1019-1031, Jan. 2024.

[3] K. T. Chau, C. C. Chan and C. Liu, "Overview of permanent-magnet brushless drives for electric and hybrid electric vehicles," *IEEE Trans. Ind. Electron.*, vol. 55, no. 6, pp. 2246-2257, June 2008.

[4] N. Bianchi, L. Alberti and M. Barcaro, "Design and tests of a four-layer fractional-slot interior permanent-magnet motor," *IEEE Trans. Ind. Appl.*, vol. 52, no. 3, pp. 2234-2240, May-June 2016.

[5] L. Dai, J. Gao, S. Niu and S. Huang, "Multi-electromagnetic performance optimization of double-layer interior permanent magnet synchronous machine," *IEEE Trans. Ind. Electron.*, vol. 71, no. 11, pp. 14535-14545, Nov. 2024.

[6] L. Dai, S. Niu, W. Zhang, J. Gao and S. Huang, "Harmonic modeling and ripple suppression of electromagnetic torque in IPMSMs," *IEEE Trans. Ind. Electron.*, vol. 71, no. 12, pp. 16223-16233, Dec. 2024.

[7] L. Dai, S. Niu, J. Gao, K. Liu, S. Huang and W. L. Chan, "Diverse slot-opening designs for cogging torque and performance optimization in PM machines," *IEEE Trans. Transp. Electrif.*, *Early Access*, doi: 10.1109/TTE.2025.3540837

[8] J. Liu, H. Li and Y. Deng, "Torque ripple minimization of PMSM based on robust ILC via adaptive sliding mode control," *IEEE Trans. Power Electron.*, vol. 33, no. 4, pp. 3655-3671, April 2018.

[9] S. A. Q. Mohammed, H. H. Choi and J. -W. Jung, "Improved iterative learning direct torque control for torque ripple minimization of surface-mounted permanent magnet synchronous motor drives," *IEEE Trans. Ind. Inform.*, vol. 17, no. 11, pp. 7291-7303, Nov. 2021.

[10] P. Mattavelli, L. Tubiana, and M. Zigliotto, "Torque-ripple reduction in PM synchronous motor drives using repetitive current control," *IEEE Trans. Power Electron.*, vol. 20, no. 6, pp. 1423–1431, Nov. 2005.

[11] M. Tang, A. Formentini, S. A. Odhano, and P. Zanchetta, "Torque ripple reduction of PMSMs using a novel angle-based repetitive observer," *IEEE Trans. Ind. Electron.*, vol. 67, no. 4, pp. 2689–2699, Apr. 2020.

[12] Z. Lyu, L. Wu and P. Song, "A novel harmonic current control method for torque ripple reduction of SPMSM considering dc-link voltage limit," *IEEE Trans. Power Electron.*, vol. 39, no. 2, pp. 2558-2568, Feb. 2024.

[13] Y. Ma, S. Niu, W. Fu and J. Fei, "A novel direct-drive rotary–linear machine and ripple reduction by harmonic current injection approach," *IEEE Trans. Power Electron.*, vol. 38, no. 12, pp. 15272-15286, Dec. 2023.

[14] J. Qu, J. Jatskevich, C. Zhang and S. Zhang, "Torque ripple reduction method for permanent magnet synchronous machine drives with novel harmonic current control," *IEEE Trans. Energy Convers.*, vol. 36, no. 3, pp. 2502-2513, Sept. 2021.

[15] G. Feng, C. Lai and N. C. Kar, "An analytical solution to optimal stator current design for pmsm torque ripple minimization with minimal machine losses," *IEEE Trans. Ind. Electron.*, vol. 64, no. 10, pp. 7655-7665, Oct. 2017.

[16] G. Feng, C. Lai, and N. C. Kar, "Practical testing solutions to optimal stator harmonic current design for PMSM torque ripple minimization using speed harmonics," *IEEE Trans. Power Electron.*, vol. 33, no. 6, pp. 5181–5191, Jun. 2018.

[17] L. Yan, Y. Liao, H. Lin, and J. Sun, "Torque ripple suppression of permanent magnet synchronous machines by minimal harmonic current injection, " *IET Elect. Power Appl.*, vol. 12, no. 6, pp. 1368-1375, May 2019.

[18] G. Feng, C. Lai, X. Tan, B. Wang and N. C. Kar, "Optimal current modeling and identification for fast and efficient torque ripple minimization of PMSM using theoretical and experimental models," *IEEE Trans. Ind. Electron.*, vol. 68, no. 12, pp. 11806-11816, Dec. 2021, doi: 10.1109/TIE.2020.3047058.

[19] L. Dai, S. Niu and X. Yuan, "Current-Injected Torque Ripple Reduction With Minimized Iron Loss in PMSMs," *IEEE Trans. Ind. Electron.*, vol. 72, no. 9, pp. 9790-9794, Sept. 2025.

[20] B. Zheng, J. Zou, Y. Xu, X. Lang and G. Yu, "Torque ripple suppression based on optimal harmonic current injection in dual three-phase PMSMs under magnetic saturation," *IEEE Trans. Ind. Electron.*, vol. 69, no. 6, pp. 5398-5408, June 2022.

[21] C. Lai, G. Feng, K. Mukherjee, V. Loukanov, and N. C. Kar, "Torque ripple modeling and minimization for interior PMSM considering magnetic saturation," *IEEE Trans. Power Electron.*, vol. 33, no. 3, pp. 2417–2429, Mar. 2018.

[22] J. Qu, P. Zhang and J. Jatskevich, "Harmonic current optimization for torque ripple reduction in permanent magnet synchronous machine drives based on torque ripple surrogate model," *IEEE Trans. Power Electron.*, vol. 39, no. 5, pp. 5108-5120, May 2024.

[23] J. Qu, P. Zhang, C. Zhang and S. Zhang, "Torque ripple reduction method for interior permanent magnet synchronous machine drives with minimal loss," 2022 IEEE Energy Conversion Congress and Exposition (ECCE), Detroit, MI, USA, 2022, pp. 1-7.

[24] Jeong-Soo Park, "Optimal Latin-hypercube designs for computer experiments," *Journal of Statistical Planning and Inference*, vol. 39, Issue 1, Pages 95-111, April 1994.

[25] Man-Wai Mak and Sun-Yuan Kung, "Estimation of elliptical basis function parameters by the EM algorithm with application to speaker verification," *IEEE Trans. Neural Netw.*, vol. 11, no. 4, pp. 961-969, July 2000.

[26] K. Deb, A. Pratap, S. Agarwal and T. Meyarivan, "A fast and elitist multiobjective genetic algorithm: NSGA-II," *IEEE Trans. Evol. Comput.*, vol. 6, no. 2, pp. 182-197, April 2002.

[27] J. Xu, S. Guo, H. Guo and X. Tian, "Fault-tolerant current control of six-phase permanent magnet motor with multifrequency quasi-proportional-resonant control and feedforward compensation for aerospace drives," *IEEE Trans. Power Electron.*, vol. 38, no. 1, pp. 283-293, Jan. 2023.

[28] S. -H. Park, J. -C. Park, S. -W. Hwang, J. -H. Kim, H. -J. Park and M. -S. Lim, "Suppression of torque ripple caused by misalignment of the gearbox by using harmonic current injection method," *IEEE/ASME Trans. Mech.*, vol. 25, no. 4, pp. 1990-1999, Aug. 2020.

Litao Dai (Member, IEEE) was born in Changsha, China, in 1993. He received the B.S. degree in mathematics from Harbin University of Commerce, Harbin, China, in 2015, and Ph.D. degree in electrical engineering from Hunan University, Changsha, China, in 2023.

He is currently working as a Postdoctoral Fellow with the Department of Electrical and Electronic Engineering, The Hong Kong Polytechnic University, Hong Kong, SAR, China.

Shuangxia Niu (Senior Member, IEEE) received the B.Sc. and M.Sc. degrees from Tianjin University, Tianjin, China, in 2002 and 2005, and the Ph.D. degree from the University of Hong Kong, Hong Kong, SAR, China, in 2009, all in electrical engineering.

She is currently a professor with the Department of Electrical and Electronic Engineering, The Hong Kong Polytechnic University. She authored or coauthored more than 200 papers in leading journals. Prof. Niu is currently an Associate Editor of the IEEE Transactions on Industrial Electronics and the IEEE Journal of Emerging and Selected Topics in Power Electronics.

Xin Yuan (S'19-M'20) received a B.Sc. degree in electrical engineering and automation from Beijing Union University in 2013 and received an M.Phil. degree in electrical engineering from North China University of Technology in 2016. In 2020, he received a Ph.D. in electrical engineering from the Beijing Institute of Technology, Beijing, China.

He joined the Department of Electronic & Electrical Engineering at the University of Strathclyde in 2025, worked as a Senior Lecturer (Associate Professor). Before joining the University of Strathclyde, He worked as a Lecturer (Assistant Professor) at the School of Engineering of the University of Aberdeen, Research Assistant Professor at the Department of

Electrical and Electronic Engineering of Hong Kong Polytechnic University, Hong Kong, and Research Associate at the PEMC Group of the University of Nottingham, UK. In 2020, he received a Ph.D. in electrical engineering from the Beijing Institute of Technology, Beijing, China, and he was also a Postdoctoral Research Fellow with the School of Electrical and Electronic Engineering, Nanyang Technological University, Singapore, from 2020 to 2022. He was a World's Top 2% Most-cited Scientist by Stanford University in 2024 and received several external research grants in Hong Kong and the UK, including the UK-Royal Society, HK-ITF and EU-Horizon Europe funding agencies. He has more than 15 years of experience working on DC/AC, DC/DC, and AC/DC power conversion and his research interests include electric vehicle, electric ship, wind turbine, and aircraft transportation applications. His speciality mainly contains the high-efficiency/fault-tolerant/low switching frequency/EMI suppression AC machine control and high-power density integrated multilevel WBG power converter hardware design with EMI suppression. Dr. Yuan has published over 50 academic papers and 4 patents, and served as a Guest Editor, Technical Track Chair, Special Session Chair, Associate Editor and Reviewer in different international journals and conferences.

C. C. Chan (Life Fellow, IEEE) was born in 1937. He received the B.S. degree from the China University of Mining and Technology, Xuzhou, China, the M.S. degree from Tsinghua University, Beijing, China, and the Ph.D. degree from The University of Hong Kong, Hong Kong, in 1957, 1959, and 1982, respectively, all in electrical engineering.

He has more than 50 years of teaching and research experience and proposes engineering philosophy, engineering and education innovation, which laid the foundation of modern electric vehicles theory and electric vehicles electric drive theory. He has authored more than 300 papers and 11 monographs.

Dr. Chan is a Member of Chinese Academy of Engineering, Fellow of the Royal Academy of Engineering U.K., Member of Ukrainian Academy of Engineering Sciences, and Honorary Fellow of Hungarian Academy of Engineering. He is a Senior IET Fellow, and the former President of the Hong Kong Institution of Engineers. He was the recipient of the Toastmasters Medal by the Institution of Electrical Engineers (IEE) in 2000, “Father of Asian Electric Vehicles” by Magazine Global View in 2003, “Environmental Excellence in Transportation Award” by the Society of Automotive Engineers (SAE) in 2007, Gold Medal of Hong Kong Institution of Engineers in 2010, World Federation of Engineering (WFEO) Medal for Engineering Excellence in 2013, Prince Philip Medal of U.K. Royal Academy of Engineering in 2014, and “IEEE Transportation Technologies Award” by the Institute of Electrical and Electronics Engineers (IEEE) in 2018.